The Astrophysical Journal, 967:71 (9pp), 2024 May 20 https://doi.org/10.3847/1538-4357/ad3960

Modeling the Saturation of the Bell Instability Using Hybrid Simulations

Georgios Zacharegkas[1,2], Damiano Caprioli[3,4], Colby Haggerty[5], Siddhartha Gupta[3,6], and Benedikt Schroer[3]
[1] High-Energy Physics Division, Argonne National Laboratory, Argonne, IL 60439, USA
[2] Kavli Institute for Cosmological Physics, University of Chicago, Chicago, IL 60637, USA
[3] Department of Astronomy & Astrophysics, University of Chicago, Chicago, IL 60637, USA
[4] Enrico Fermi Institute, The University of Chicago, Chicago, IL 60637, USA
[5] Institute for Astronomy, University of Hawaii, Honolulu, HI 96822, USA
[6] Department of Astrophysical Sciences, Princeton University, 4 Ivy Ln., Princeton, NJ 08544, USA
Received 2024 January 16; revised 2024 March 21; accepted 2024 March 30; published 2024 May 20

Abstract

The nonresonant streaming instability (Bell instability) plays a pivotal role in the acceleration and confinement of cosmic rays (CRs), yet the exact mechanism responsible for its saturation and the magnitude of the final amplified magnetic field have not been assessed from first principles. Using a survey of hybrid simulations (with kinetic ions and fluid electrons), we study the evolution of the Bell instability as a function of the parameters of the CR population. We find that at saturation, the magnetic pressure in the amplified field is comparable with the initial CR anisotropic pressure, rather than with the CR energy flux, as previously argued. These results provide a predictive prescription for the total magnetic field amplification expected in the many astrophysical environments where the Bell instability is important.

Unified Astronomy Thesaurus concepts: Cosmic rays (329); Galactic cosmic rays (567); Particle astrophysics (96); Cosmic ray sources (328); High-energy cosmic radiation (731); High energy astrophysics (739); Plasma astrophysics (1261)

1. Introduction

Collisionless shock waves associated with supernova remnants (SNRs) are believed to be the primary source of Galactic cosmic rays (CRs; up to "knee" rigidities of $\sim 10^{15}$ V), through the Diffusive Shock Acceleration (DSA) mechanism (Bell 1978; Blandford & Ostriker 1978). However, for efficient CR acceleration through DSA, CRs must be confined close to the shock, which requires the presence of very strong, turbulent magnetic fields (Lagage & Cesarsky 1983; Blasi et al. 2007). Strong magnetic turbulence and CR acceleration are thus closely related and the study of the growth and saturation of such strong magnetic fields is crucial to explaining the origin of high-energy CRs.

Winske & Leroy (1984) originally found that in systems with a sufficiently strong CR current, right-handed modes with wavelengths significantly smaller than the CR gyroradius could be excited; these modes differ from the linearly polarized ones driven by the resonant CR streaming instability, which is caused by CRs in gyroresonance with Alfvénic modes (Kulsrud & Pearce 1969; Zweibel 1979; Achterberg 1983). Historically, only the resonant modes were believed to be important, because of the gyroresonance condition for CR scattering; the nonresonant branch was ignored until Bell (2004) showed that the right-handed modes grow faster than left-handed ones and —most importantly—that they can grow to nonlinear levels, eventually saturating at large amplitudes. This claim was motivated by simulations that couple a magnetohydrodynamical (MHD) description of the thermal plasma with a kinetic treatment of the CR current (Lucek & Bell 2000; Bell & Lucek 2001). The *nonresonant streaming instability*, often referred to as the "Bell instability," occurs in many space/astrophysical environments, and in particular is crucial for the production of high-energy CRs in SNRs, as attested by global kinetic simulations of nonrelativistic shocks (e.g., Caprioli & Spitkovsky 2013, 2014a, 2014b, 2014c; Crumley et al. 2019; Marcowith et al. 2021), as well as for the dynamics of the shocks themselves (e.g., Caprioli et al. 2020; Haggerty & Caprioli 2020).

1.1. Linear Theory and Modifications

The linear theory for the Bell instability shows that the instability is expected to grow faster than the resonant instability when the maximally unstable wavelength, of wavenumber $k_{\rm max}$, is much smaller than the CR gyroradius r_L, i.e., $k_{\rm max} r_L \gg 1$; we comment on such a condition extensively in what follows.

In this regime, right-handed circularly polarized modes are driven unstable and grow faster than their resonant (left-handed) counterparts, as shown, e.g., in Section 4.3 of Bell (2004) and Section 3 of Amato & Blasi (2009). The wavenumber of the fastest-growing mode is

$$k_{\rm max} = \frac{2\pi}{c}\frac{J_{\rm cr}}{B_0} = \frac{1}{2}\left(\frac{n_{\rm cr}}{n_{\rm g}}\right)\left(\frac{v_{\rm d}}{v_{\rm A,0}}\right) d_i^{-1}\,, \tag{1}$$

and its corresponding growth rate reads

$$\gamma_{\rm max} = k_{\rm max} v_{\rm A,0} = \frac{1}{2}\left(\frac{n_{\rm cr}}{n_{\rm g}}\right)\left(\frac{v_{\rm d}}{v_{\rm A,0}}\right)\Omega_{ci}, \tag{2}$$

where e and m are the proton charge and mass, $J_{\rm cr} = e n_{\rm cr} v_{\rm d}$ is the CR current, $n_{\rm cr}$ and $v_{\rm d}$ are the CR number density and drift velocity relative to the background plasma, B_0 and $n_{\rm g}$ are the background magnetic field and plasma number density, $v_{\rm A,0} \equiv B_0/\sqrt{4\pi m n_{\rm g}}$ is the initial Alfvén speed, $\Omega_{ci} \equiv eB_0/(mc)$

is the ion gyrofrequency, and $d_i \equiv v_{A,0}/\Omega_{ci}$ is the ion inertial length.

It is important to point out that a current of energetic particles may also drive a plethora of additional modes, both parallel and transverse to the magnetic field (e.g., Bykov et al. 2011; Malovichko et al. 2015), as discussed in the thorough review by Bret (2009), where the growth rates of Weibel, two-stream, Buneman, filamentation, Bell, and cyclotron instabilities are compared for different CR parameters. While these instabilities may be important in some environments, especially at scales smaller than the ion skin depth, global kinetic simulations of strong shocks confirm that Bell amplification is the most prominent way of producing the turbulence responsible for the acceleration of CRs to higher and higher energies (e.g., Caprioli & Spitkovsky 2014a, 2014b; Caprioli et al. 2018; Haggerty & Caprioli 2019; Marcowith et al. 2021).

The original derivation of the growth rate of the Bell instability did not account for situations where the background plasma is not strictly cold or collisionless. The Bell instability is expected to be modified when the background plasma is sufficiently warm; in this regime (dubbed "WICE," for warm ions/cold electrons), the fastest-growing wavenumber shifts to $k_{\rm wice} < k_{\rm max}$ and the growth rate is suppressed (Reville et al. 2008; Zweibel & Everett 2010; Marret et al. 2021). Additionally, the instability is modified in systems where the collisional timescale becomes comparable to the growth rate (Reville et al. 2007). Systems with proton-neutral collisions were found to have reduced growth rates and saturated magnetic field amplitudes, while systems with proton–proton collisions resulted in a larger saturated magnetic field, owing to the suppression of temperature anisotropy generation (Marret et al. 2022). While these considerations are potentially important for selecting systems, they are not included in the present work.

1.2. Simulating the Bell Instability

MHD simulations have shown that for a fixed CR current, large amplification factors can be achieved (e.g., Bell 2004, 2005; Zirakashvili et al. 2008; Matthews et al. 2017). Nevertheless, these simulations cannot self-consistently capture the backreaction of the growing modes on the CRs, hence they cannot be used to assess the saturation of the Bell instability.

Using particle-in-cell (PIC) simulations, Niemiec et al. (2008) found a much lower level of amplitude of the saturated magnetic field, but they also found a growth rate for the fastest-growing mode that was smaller than what Bell (2004) had predicted, putting into question the existence of the Bell instability beyond the MHD limit. However, PIC simulations performed by Riquelme & Spitkovsky (2009) showed that for the exceedingly strong currents adopted in the work of Niemiec et al. (2008), a transverse filamentary mode can grow faster than the Bell instability; they also found that for typical CR currents, the Bell instability grows as expected and saturates to levels of $\delta B/B_0 \gtrsim 10$. The saturation was found to be caused by the background plasma being accelerated in the direction of the CR drift velocity, which reduces the CR current $\boldsymbol{J}_{\rm cr}$ that drives the instability. Similar results have been found in the PIC simulations performed by other groups as well (Ohira et al. 2009; Stroman et al. 2009; Gupta et al. 2021).

Gargaté et al. (2010) and Weidl et al. (2019a, 2019b) used hybrid simulations (with kinetic ions and fluid electrons) to follow the instability on longer timescales, well into the nonlinear regime when saturation occurs. Their results supported a saturation mechanism similar to that described by Riquelme & Spitkovsky (2009), who used full PIC simulations: saturation occurs due to the deceleration of CRs and simultaneous acceleration of the background plasma, which reduces the CR current, an effect also seen in the earlier work of Lucek & Bell (2000).

The vast majority of the studies above were performed in 2D periodic boxes, with a CR current initialized but not sustained (*undriven simulations*), while in astrophysical environments a parcel of fluid, e.g., in a shock precursor, is constantly exposed to "fresh" CRs. To mimic this more physical situation, Reville & Bell (2013) used an MHD+Vlasov code, where the CR distribution function is expanded in spherical harmonics satisfying a Fokker–Planck equation to run *driven simulations*, in which the CR current is enforced to be constant. In their simulations, the maximum value of the magnetic field is always time-limited, and no final saturation of the magnetic field was reported.

Kobzar et al. (2017) performed one full PIC 2D simulation in a nonperiodic box, which allowed the authors to follow the spatiotemporal evolution of the instability; however, the relatively high current that they used led to the formation of a shock and in general does not allow for the construction of a theory for arbitrary CR distributions.

In this paper, we study the Bell instability via hybrid simulations using the massively parallel code `dHybridR` (Gargaté et al. 2007; Haggerty & Caprioli 2019), where ions are treated kinetically and their relativistic dynamics is retained. We perform *driven simulations*, in which CRs are injected in the simulation box at a constant rate from the left side and are free to leave from the right, while the thermal background plasma and the electromagnetic fields are subject to periodic boundary conditions. This setup allows for a self-consistent coupling between CRs and thermal plasma, which eventually leads to the saturation of the instability. We explore a large range of parameters that characterize the CR current, always in the regime in which Bell is the fastest-growing instability, and we use a suite of 1D, 2D, and 3D simulations to investigate how the amplified magnetic field at saturation scales with the CR parameters.

We study the nonlinear evolution of the driven Bell instability and provide the first simulation-validated prescription for the level of the final magnetic field at saturation, i.e., that the final magnetic pressure is comparable to the initial net CR momentum flux.

The structure of the paper is as follows. In Section 2, we briefly outline the possible CR distributions that may trigger the Bell instability and parameterize their free energy. Section 3 describes our computational setup, the explored parameter space, and discusses the time evolution of a benchmark simulation. In Section 4, we then describe the properties of the system at saturation and present the scaling of the total amplified magnetic field with the initial CR momentum flux. Finally, in Section 5, we discuss our results in the context of the current literature and outline some astrophysical implications of our findings, before concluding in Section 6.

2. The Free Energy in Streaming CRs

Let us consider a population of CRs with isotropic monochromatic momentum $p_{\rm iso} \equiv \gamma_{\rm iso} m v_{\rm iso}$ in their rest frame, which drift with velocity $\boldsymbol{v}_{\rm d} = v_{\rm d}\hat{\boldsymbol{e}}_x$ relative to the thermal plasma; this corresponds to a current $\boldsymbol{J}_{\rm cr} = e n_{\rm cr} \boldsymbol{v}_{\rm d}$, where $n_{\rm cr}$

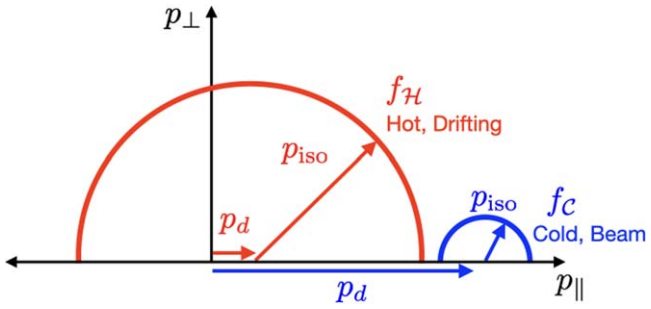

Figure 1. Schematic diagram of the initial CR distributions, distinguishing the hot and cold cases (also see Table 1).

represents the CR number density measured in the rest frame of the thermal plasma.

Let us fix the initial magnetic field $\boldsymbol{B} = B_0\hat{\boldsymbol{e}}_x$; its inclination with respect to $\boldsymbol{v}_{\rm d}$ should not be important for the growth or the saturation of the Bell instability (e.g., Bell 2005; Matthews et al. 2017). More specifically, the inclination may change the growth rate along the parallel and perpendicular directions, $k_\parallel$ and $k_\perp$, respectively, with respect to $\hat{\boldsymbol{e}}_x$, but the saturated magnetic field's amplitude may not change.

While the CR current and hence the growth rate only depend on $n_{\rm cr}$ and $v_{\rm d}$, the net CR momentum and energy fluxes depend on $p_{\rm iso}$, too. We consider two limiting cases: one in which the CRs are a *cold beam* with $p_{\rm d} \gg p_{\rm iso}$ and one in which they have a *hot-drifting* distribution with $p_{\rm d} \ll p_{\rm iso}$, as illustrated in Figure 1.

2.1. Bell's Prescription for Saturation

According to the standard theory (Bell 2004; Amato & Blasi 2009), the right-handed, nonresonant modes grow faster than the resonant one if

$$k_{\rm max} r_{\rm L} = \frac{n_{\rm cr}}{n_{\rm g}} \frac{v_{\rm d}}{v_{\rm A,0}} \frac{p_\perp}{m v_{\rm A,0}} \equiv \xi_{\rm Bell} \gg 1, \tag{3}$$

where $r_L(p_\perp)$ is the typical CR gyroradius.

Bell (2004) suggested that the instability saturates when the most unstable mode, calculated in the amplified field δB, becomes resonant with the CRs, i.e., $k_{\rm max}(\delta B) r_{\rm L}(\delta B) \sim 1$. This is realized when

$$\left(\frac{\delta B}{B_0}\right)^2 \approx \gamma_{\rm iso} \frac{n_{\rm cr}}{n_{\rm g}} \frac{v_{\rm d} c}{v_{\rm A,0}^2} \equiv \frac{U_{\rm cr}}{U_{\rm B}} \frac{v_{\rm d}}{2c} = \xi_{\rm Bell}, \tag{4}$$

where $U_{\rm cr} \equiv \gamma_{\rm iso} m n_{\rm cr} c^2$ and $U_{\rm B} \equiv m n_{\rm g} v_{\rm A}^2/2$ are the CR and magnetic energy densities, assuming that CRs are relativistic and $v_{\rm d}$ is not; at saturation, one then has $\delta B^2/B_0^2 \approx \xi_{\rm Bell}$. Blasi et al. (2015) came to a similar conclusion with an argument based on the dynamical balance between the magnetic tension and the $\boldsymbol{J}_{\rm cr} \times \boldsymbol{B}$ force.

With regard to Equation (4), note that (1) it is only *similar* to the ratio of CR and magnetic energy fluxes (the denominator is *not* the magnetic energy flux, because waves do not move at c); (2) it holds in the limit in which CRs are relativistic and the drift is not, since the $p_\perp$ that enters $r_{\rm L}$ is effectively $p \approx \gamma_{\rm iso} mc$; and (3) it has never been validated by means of self-consistent kinetic simulations.

For relativistic CRs, energy and momentum are essentially interchangeable, but for nonrelativistic particles, or nonrelativistic drifts, that is not the case. Thus, it would be desirable to have a relativistically covariant expression that expressed the field at saturation for an arbitrary CR distribution.

2.2. A Covariant Formalism

We start by considering the CR rest frame, where the CR mass density is $\tilde{\rho}_{\rm cr}$, the total (including the rest mass) energy density is $e_{\rm cr} = \gamma_{\rm iso}\tilde{\rho}_{\rm cr}c^2$, and the isotropic pressure reads $P_{\rm cr} = \frac{1}{3}\gamma_{\rm iso}\tilde{\rho}_{\rm cr}c^2\beta_{\rm iso}^2$. Then we boost such a distribution into a frame that moves with velocity $\boldsymbol{v}_{\rm bst}$ and has a corresponding Lorentz factor $\Gamma_{\rm bst} = 1/\sqrt{1 - v_{\rm bst}^2/c^2}$. In this frame, the CR density is $\rho_{\rm cr} = \Gamma_{\rm bst}\tilde{\rho}_{\rm cr}$ and the CR stress tensor reads (see, e.g., Section 133 of Landau & Lifshitz 1987)

$$T^{\alpha\beta} = (e_{\rm cr} + P_{\rm cr}) u_{\rm bst}^\alpha u_{\rm bst}^\beta + P_{\rm cr}\eta^{\alpha\beta}, \tag{5}$$

where $u_{\rm bst}^\alpha$ is the four-velocity constructed with $\boldsymbol{v}_{\rm bst}$ and $\eta^{\alpha\beta}$ is the Minkovski metric. Explicitly, in components we have:

$$T^{00} = \gamma_{\rm bst}^2 (e_{\rm cr} + P_{\rm cr}) - P_{\rm cr},$$

$$T^{0i} = T^{i0} = \gamma_{\rm bst}^2 (e_{\rm cr} + P_{\rm cr}) \frac{v_{\rm bst}^i}{c},$$

$$T^{ij} = \gamma_{\rm bst}^2 (e_{\rm cr} + P_{\rm cr}) \frac{v_{\rm bst}^i v_{\rm bst}^j}{c^2} + P_{\rm cr}\delta^{ij},$$

where $i, j = 1, 2, 3$ and δ^{ij} is the Kronecker delta symbol. Here, T^{00} has the usual meaning of energy density, while T^{ij} is the flux along the i direction of density of momentum p_j; T^{0i} does not have a nonrelativistic counterpart, though T^{0i}/c and cT^{0i} are the density of momentum along i and the energy flux along i, respectively.

Note that if CRs are relativistic, then the drift velocity $v_{\rm d}$ that enters the CR current is generally *smaller* than $v_{\rm bst}$ (Gupta et al. 2021), i.e.,

$$v_{\rm d} = \frac{1}{2}\int_{-1}^{1} d\mu \frac{\mu v_{\rm iso} + v_{\rm bst}}{1 + \mu v_{\rm iso} v_{\rm bst}/c^2} \leqslant v_{\rm bst}, \tag{6}$$

where $v_x = \mu|\boldsymbol{v}|$. Since the simulations are set up with an effective boost to the background plasma frame, we will provide the saturation as a function of $v_{\rm bst}$ rather than $v_{\rm d}$. Also, the average momentum along x reads

$$\langle p_{{\rm cr},x} \rangle = \frac{\gamma_{\rm bst}}{2}\int_{-1}^{1} d\mu (\mu p_{\rm iso} + \gamma_{\rm iso} m v_{\rm bst}) = \gamma_{\rm iso} p_{\rm bst}. \tag{7}$$

The questions that arise then are (1) can the saturation of the Bell instability be connected to the initial CR distribution? And (2) which component(s) of $\boldsymbol{T}$ is the saturation of the Bell instability related to?

In general, to drive the instability, we need a finite current (i.e., charge flux), which also means a net momentum and energy flux. We consider the following quantity:

$$\xi_0 \equiv \frac{T^{11} - P_{\rm cr}}{P_{B,0}} = \frac{T^{01}}{P_{B,0}} \frac{v_{\rm bst}}{c} = \frac{T^{00} - \tilde{\rho}_{\rm cr}c^2}{P_{B,0}}$$

$$= 2\gamma_{\rm iso}\gamma_{\rm bst} \frac{n_{\rm cr}}{n_{\rm g}} \frac{v_{\rm bst}^2}{v_{\rm A,0}^2} \left(1 + \frac{1}{3}\frac{v_{\rm iso}^2}{c^2}\right), \tag{8}$$

which expresses the *net* CR momentum flux (consider the terms with T^{11} and T^{01}), normalized to the magnetic pressure; the last equality derives from the definition of $\boldsymbol{T}$ and expresses the density

in kinetic energy in the CR drift (the term with T^{00}).[7] In the limit considered in Equation (4) (ultrarelativistic CRs and nonrelativistic drift), from Equation (8) one has $\xi_0/\xi_{\rm Bell} \sim v_{\rm d}/c \ll 1$, which suggests that a system may run out of free momentum before the field can saturate at equipartition of the CR and magnetic fluxes.

3. Hybrid Simulations

We perform hybrid kinetic PIC simulations with `dHybridR`, in which the ions are treated as macroparticles governed by the relativistic Lorentz force and the electrons are a massless, charge-neutralizing fluid (Haggerty & Caprioli 2019). The parameters of the different runs are listed in Table 1 and cover our benchmark run $\mathcal{B}$, several cold and hot CR distribution functions (see Figure 1, runs $\mathcal{C}$ and $\mathcal{H}$, respectively), as well as 1D and 3D versions of our benchmark (runs $\mathcal{D}$) and nonrelativistic CRs (runs $\mathcal{N}$). The parameters are chosen in such a way that Bell dominates over the resonant streaming instability ($\xi_0 \gg 1$) and over the filamentary instability of Niemiec et al. (2008; $\gamma_{\rm max} \ll \omega_c$).

All simulations retain all three components of the velocity and fields.

Periodic boundary conditions are imposed for fields and thermal particles, while CRs experience periodic boundary conditions in the perpendicular ($\perp$) directions and open along the parallel ($\parallel$) x-direction. This configuration mimics a system in which energetic CRs are being continuously injected, such as in a shock precursor (Reville & Bell 2013; Caprioli & Spitkovsky 2014b).

In most of the runs, the speed of light is $c = 100\, v_{\rm A,0}$, except for the nonrelativistic beam runs ($\mathcal{N}1-3$), where it is $c = 500\, v_{\rm A,0}$. The spatial resolution is two cells per ion skin depth and the time step is chosen to ensure that the Courant condition is satisfied. Since we limit ourselves to cases in which the growth rate is $\gamma \lesssim \Omega_{ci}$, $k_{\rm max} d_i \lesssim 1$ and the fastest-growing mode is always resolved.

We initialize the simulation box with four particles per cell for both background gas particles and CRs. Finally, electrons are assumed to behave like a perfect fluid with adiabatic index of $5/3$ (see, e.g., Caprioli et al. 2018).

We checked the convergence of our results as a function of number of particles per cell, space/time resolution, and box size, finding that the minimum required box size must be larger than at least one CR gyroradius in the initial magnetic field. Since it is notoriously difficult to deal with hot (i.e., subsonic) distributions close to open boundaries, for hot CR distributions we consider much larger computational boxes and perform our saturation analysis only in the center of the box, effectively avoiding any boundary effect.

3.1. The Benchmark Run

We now discuss the benchmark run ($\mathcal{B}$ in Table 1) to outline the features that are common to all of the simulations. As expected, CRs drive magnetic field perturbations that grow exponentially on a timescale $\sim\gamma_{\rm max}^{-1}$ (e.g., Riquelme & Spitkovsky 2009; Gargaté et al. 2010; Haggerty et al. 2019). Figure 2 shows how the magnetic structures grow in size and intensity. Initially, such structures are much smaller than the CR gyroradius, represented by a white circle; both the growth rate and maximally unstable wavelength are consistent with the linear theory predictions. After a few to ten growth times, they become comparable to the CR gyroradii calculated in the amplified magnetic field $\gtrsim 10\, B_0$ (last panels).

It is interesting to look at the evolution of the first and second moments (bulk velocity and pressure) of the CR and gas distributions, indicated with u_s and P_s, with $s = $ CR, gas, respectively. When $\delta B/B_0$ exceeds unity ($t \sim 5\gamma_{\rm max}^{-1}$), CRs start scattering off the magnetic perturbations and transfer momentum to the background gas. As a result, we see an abrupt initial drop in the CR bulk velocity, while the gas is set in motion in the direction of the CR drift, as discussed, e.g., by Weidl et al. (2019a, 2019b). At saturation, the CRs and gas are

Table 1
List of the Simulations Used in the Work, Defined by: the CR Number Density, $n_{\rm cr}$; the Parallel CR Momentum Boost, $p_{\rm bst}$; the Initial Isotropic Momentum, $p_{\rm iso}$; and ξ_0, the CR Net Momentum Flux (see Equation (8))

Run	$n_{\rm cr}/n_{\rm g}$	$p_{\rm bst}/(mv_{\rm A,0})$	$p_{\rm iso}/(mv_{\rm A,0})$	ξ_0
$\mathcal{B}$	10^{-3}	10^3	1	195
$\mathcal{B}2$	5×10^{-4}	10^3	1	98
$\mathcal{C}1$	10^{-3}	1.5×10^3	1	293
$\mathcal{C}2$	10^{-3}	5×10^2	1	96
$\mathcal{C}3$	10^{-3}	2×10^3	1	392
$\mathcal{C}4$	10^{-3}	7.5×10^2	1	146
$\mathcal{C}5$	10^{-3}	10^4	1	1960
$\mathcal{C}6$	10^{-3}	5×10^3	1	980
$\mathcal{C}7$	10^{-3}	3×10^3	1	588
$\mathcal{C}8$	10^{-3}	8×10^3	1	1568
$\mathcal{C}9$	10^{-3}	2×10^2	1	35
$\mathcal{C}10$	10^{-3}	3×10^2	1	56
$\mathcal{C}11$	10^{-3}	4×10^2	1	76
$\mathcal{H}1$	10^{-3}	10^3	10^3	2601
$\mathcal{H}2$	10^{-3}	10^3	500	1312
$\mathcal{H}3$	10^{-3}	10^3	10	197
$\mathcal{H}4$	10^{-3}	10^3	50	233
$\mathcal{H}5$	10^{-3}	10^3	10^2	322
$\mathcal{H}6$	9.9×10^{-2}	3	10^3	6
$\mathcal{H}7$	3.6×10^{-2}	5	10^3	12
$\mathcal{H}8$	2.4×10^{-2}	10	500	24
$\mathcal{H}9$	6.8×10^{-3}	20	10^3	64
$\mathcal{H}10$	1.4×10^{-2}	31	400	128
$\mathcal{H}11$	8.2×10^{-3}	44	500	180
$\mathcal{H}12$	2.2×10^{-3}	58	400	64
$\mathcal{H}13$	4.2×10^{-3}	75	10^3	480
$\mathcal{H}14$	3×10^{-3}	98	10^3	520
$\mathcal{H}15$	1.5×10^{-3}	133	10^3	400
$\mathcal{H}16$	10^{-3}	206	10^3	480
$\mathcal{D}1$	10^{-3}	10^3	1	195
$\mathcal{D}3$	10^{-3}	10^3	1	195
$\mathcal{N}1$	5×10^{-3}	20	1	4
$\mathcal{N}2$	5×10^{-3}	30	1	8
$\mathcal{N}3$	5×10^{-3}	40	1	15

Note. The speed of light is $c = 100\, v_{\rm A,0}$, except for the $\mathcal{N}$ cases, where it is $c = 500\, v_{\rm A,0}$. Run $\mathcal{B}$ is our benchmark case, while runs $\mathcal{C}$ and $\mathcal{H}$ indicate cold-beam and hot-drifting cases, respectively; in all of these cases, the boxes are 2D and measure at least $10^3 \times 10^3 d_i^2$. Finally, $\mathcal{D}1$ and $\mathcal{D}3$ correspond to our quasi-1D and quasi-3D control runs and measure $10^3 \times 50\, d_i^2$ and $10^3 \times 10^3 \times 200\, d_i^3$, respectively.

[7] Technically, we expect CRs to isotropize in the wave frame moving with $v_{\rm A}$ with respect to the background plasma. Hence, the correct boost velocity to use in Equation (8) is the one that boosts the CR distribution to the wave frame rather than the background plasma frame. This modification is necessary for CR distributions with $v_{\rm d} \gtrsim v_{\rm A}$, such as our cases $\mathcal{H}6$–8 in Table 1.

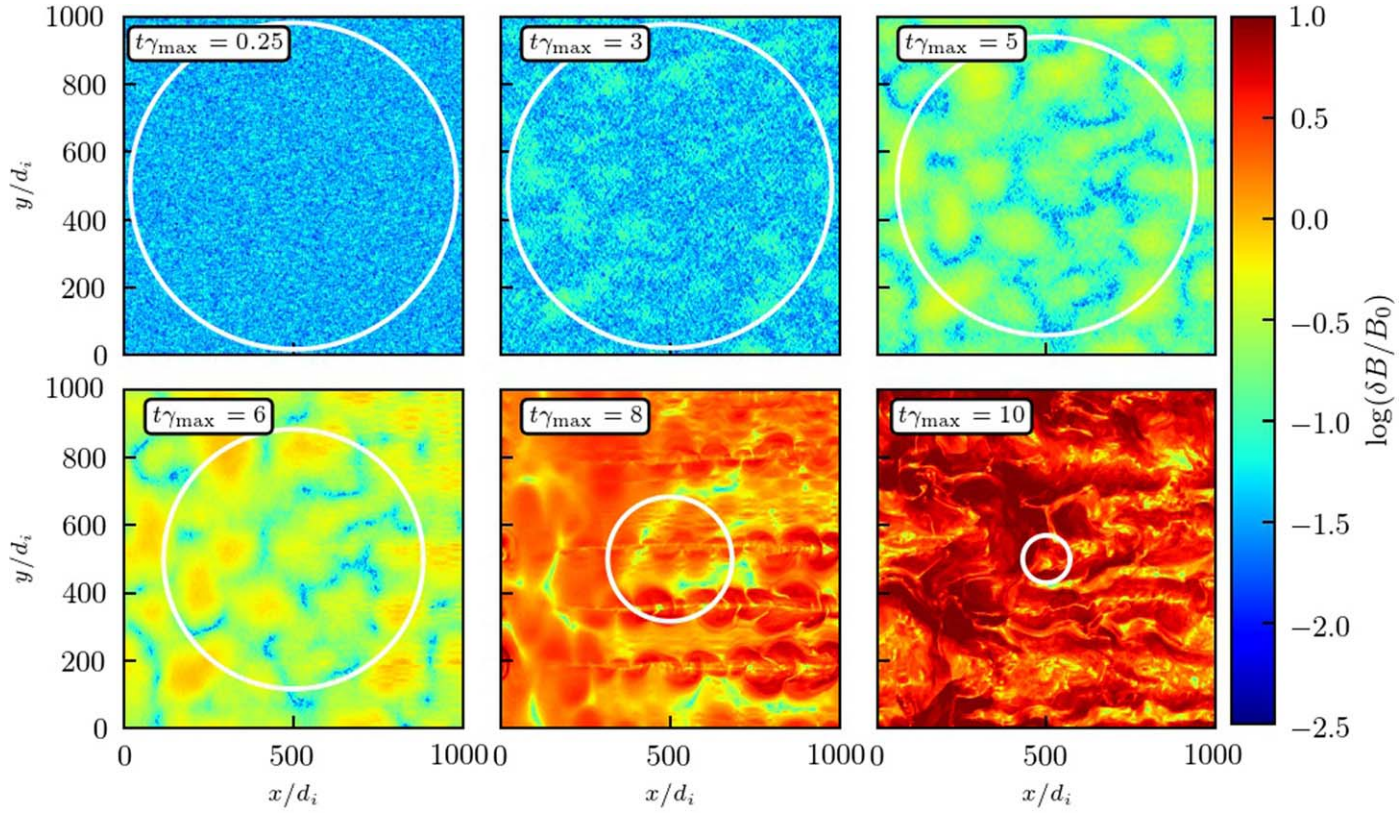

Figure 2. Time evolution of the $\log_{10}$ of the perpendicular component of the magnetic field, $\delta B = (B_y^2 + B_z^2)^{1/2}$, for our benchmark simulation (run $\mathcal{B}$ in Table 1). Time is normalized to $\gamma_{\rm max}^{-1}$ and the color scale indicates the strength of the field in units of B_0. The CR Larmor radius, defined in the amplified magnetic field, is represented by the white circles.

well coupled, and their relative speed reduces, as shown in Figure 3. More specifically, the difference between the two bulk velocities becomes comparable to the Alfvén speed in the total magnetic field at saturation (the top panel of Figure 3), which means that marginal stability is achieved. Since the CR current is driven, after the initial drop due to scattering, $J_{\rm cr\parallel}$ returns to its initial value in the simulation frame, but it keeps reducing in the gas frame (the bottom panel of Figure 3), which slows the growth rate down.

This picture is supported by Figure 4, which shows how the thermal, CR, and perpendicular (i.e., self-generated) magnetic pressures evolve in time; pressures are calculated both in the simulation and in the thermal gas frame (the top and bottom panels of the figure).

The magnetic field initially grows exponentially until $t \sim 7\ \gamma_{\rm max}^{-1}$, which marks the beginning of the "secular" stage of the instability, when B keeps growing but with a slower growth rate. During this stage, there is a rapid increase in the isotropic gas pressure; both $P_{\rm gas\perp}$ and $P_{\rm gas\parallel}$ grow until $t \sim 10\ \gamma_{\rm max}^{-1}$, when the parallel momentum flux starts becoming larger than the transverse gas pressure. The transferring of momentum from the CRs to the gas can also be seen in the slight drop of the parallel CR pressure, $P_{\rm cr\parallel}$, at $t \sim 10\ \gamma_{\rm max}^{-1}$.

This effect can be seen in more detail in Figure 5, which shows the temporal evolution of the perpendicular $(y,\ z)$ magnetic power spectrum as a function of parallel wavenumber ($k_x d_i$; top panel) and time (bottom panel). The maximum growth is consistent with the predictions, with the black dashed line marking the location of $k_{\rm max}$ (Equation (1)). The power in these modes grows over the exponential stage of the instability,

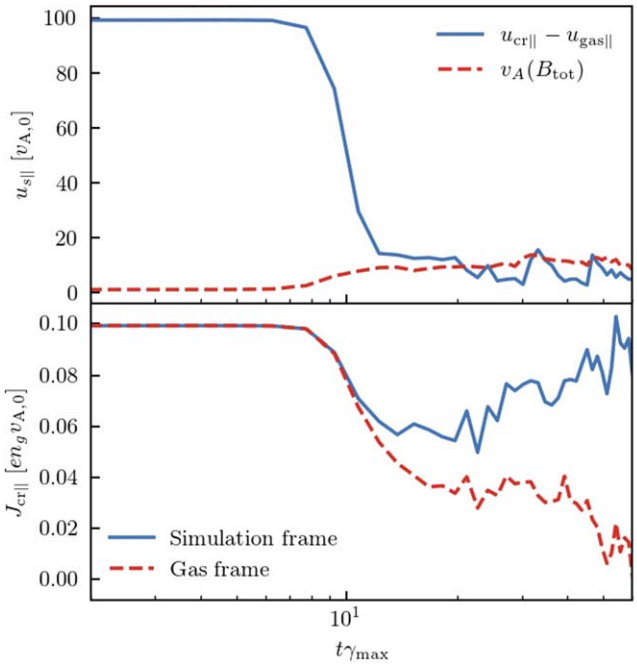

Figure 3. Top panel: time evolution of the difference between the CR and gas bulk velocities for the benchmark run $\mathcal{B}$ in Table 1, compared with the Alfvén speed in the total magnetic field. Once $\delta B/B_0 \gtrsim 1$, CRs are scattered and their bulk motion drops abruptly, while momentum is transferred to the gas; the effective CR drift speed drops and at saturation becomes comparable to $v_{\rm A}(B_{\rm tot})$, which attests to an effective coupling between CRs and thermal gas and the achievement of marginal stability. Bottom panel: CR current in both the simulation and the gas frame.

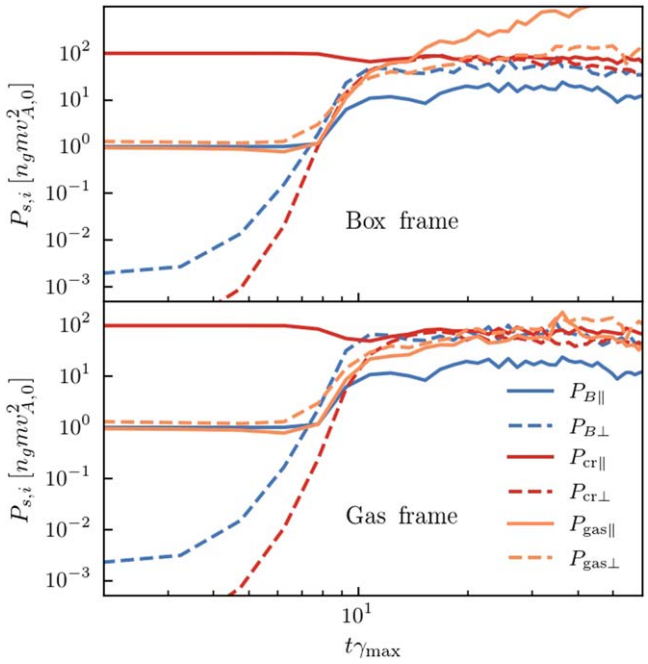

Figure 4. Evolution of the pressures of CRs, thermal gas, and magnetic field for our benchmark run $\mathcal{B}$, as seen in the simulation (top panel) or gas rest frame (bottom panel). In both panels, i denotes the direction (parallel or perpendicular) and s denotes the species (CRs, magnetic field, or gas).

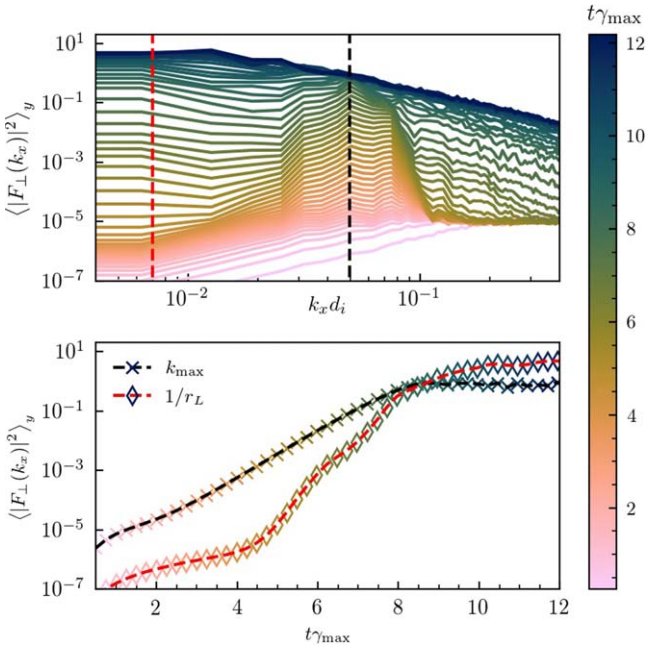

Figure 5. Top panel: transversely averaged perpendicular magnetic power spectrum $\langle |F_\perp|^2\rangle_y$, where $|F_\perp(k_x, y)|^2 = |\mathcal{F}[B_y(x, y)]|^2 + |\mathcal{F}[B_z(x, y)]|^2$ and $\mathcal{F}$ is the Fourier transform along the x-direction. The power spectrum is plotted as a function of parallel wavenumber ($k_x d_i$) for the benchmark run $\mathcal{B}$ as it evolves in time (color-coded). The black dashed line shows the predicted fastest-growing mode (Equation (1)), while the red dashed line corresponds to the mode in resonance with the CR gyroradius in the saturated magnetic field. Lower panel: time evolution of the power in the $k_{\rm max}$ mode (black dashed line, crosses) and in the resonant mode (red dashed line, diamonds). While the Bell mode grows much faster, at saturation most of the power is in quasi-resonant modes.

while in the secular phase it is the power in longer wavelengths that takes over. Such longer-wavelength modes may be as large as the CR gyroradius in the saturated magnetic field

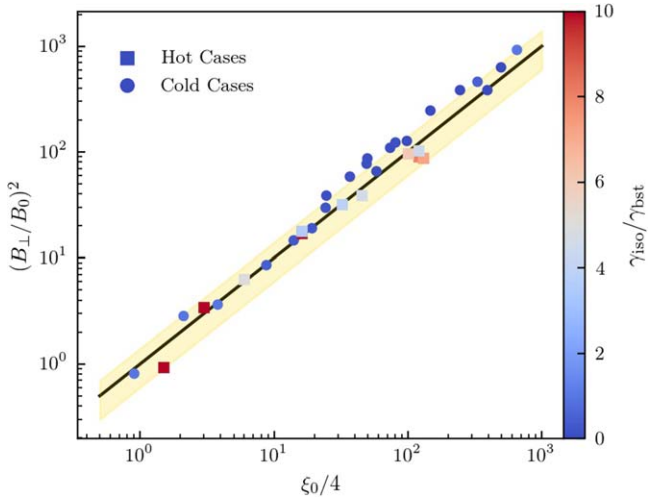

Figure 6. Transverse magnetic field at saturation, as a function of the initial CR anisotropic momentum flux normalized to the initial magnetic pressure, ξ_0 (Equation (8)). The line corresponds to $(B_\perp/B_0)^2 = \xi_0/4$. Each point represents one case from Table 1, excluding the cases $\mathcal{D}1$ and $\mathcal{D}3$ because of their different dimensionality. The gold band shades the 40% area around the line.

(red dashed line; $1/r_{\rm L}$). The power in these modes eventually surpasses that in Bell modes by the time the simulation reaches saturation, as shown in the bottom panel of Figure 5.

At $t \gtrsim 10\ \gamma_{\rm max}^{-1}$, the system reaches a state of pressure equilibrium, where $P_{\rm gas\perp} \sim P_{\rm B\perp} \sim P_{\rm cr\parallel}$. The bottom panel of Figure 4 illustrates this effect more clearly, by showing the pressures in the frame moving with the bulk velocity of the plasma, $u_{\rm gas\parallel}$. We note that the magnetic and thermal pressures grow together, suggesting that a fraction of the magnetic energy is dissipated into the background plasma, as already reported, e.g., by Bell (2004), Ohira et al. (2009), and Gargaté et al. (2010).

4. Magnetic Field at Saturation

To understand how the saturation of the nonresonant instability depends on the CR distribution, we have preformed simulations that cover a wide parameter space (Table 1). In each simulation, the parameters are selected so that we are in a regime where the Bell instability grows and dominates over any other instability. We chose to not vary the thermal speed of the background plasma, as we have found that "WICE"-like effects can be important (Reville et al. 2008; Zweibel & Everett 2010; Zacharegkas et al. 2019, 2022); we defer the study of this regime to a future work, stressing how the results presented here should apply to cases with plasma $\beta \equiv P_{\rm gas}/P_{\rm B} \ll 10$. Similarly, a large CR current ($J_{\rm cr} > en_{\rm g}v_{\rm A,0}$) may trigger two-stream, Bunemann, or filamentation instabilities (Bret 2009), a regime that we defer to future works as well.

4.1. A Simulation-validated Prescription for Magnetic Fields at Saturation

The amplitude of the transverse magnetic field at saturation is shown in Figure 6 for many hot/cold runs (color-coded), as a function of the normalized net CR momentum flux defined in Equation (8). The black line corresponds to

$$\frac{B_\perp^2}{B_0^2} = \frac{\xi_0}{4} \Leftrightarrow P_{B,\perp} = \frac{\xi_0}{4} P_{B,0}, \tag{9}$$

indicating that ξ_0 is a good parameter for estimating the total magnetic field amplification produced by generic CR distributions. This result should apply in all the cases in which the Bell modes grow faster than the resonant cyclotron instability ($k_{\rm max} r_{\rm L} \simeq \xi_{\rm Bell} \gg 1$). Also, it may apply even in the presence of instabilities (e.g., Weibel, two-stream, etc.) that grow faster than Bell, but at scales small enough that when their fastest-growing modes saturate, the CR current is not strongly affected and is still able to drive Bell modes. This would be similar to what happens for the Bell instability, in that at saturation most of the magnetic power is never on scales comparable to $k_{\rm max}$, but rather on scales of the order of the CR gyroradius, as shown in Figure 5.

As our new prescription shows, the relevant quantity is the CR momentum flux ξ_0, rather than the CR current itself, which means that saturation does not necessarily correlate with growth rate. One nontrivial implication of this finding is that the same electric current made of more energetic CRs should result in a larger magnetic field amplification, which may be relevant for CRs escaping their sources (e.g., Cristofari et al. 2021; Schroer et al. 2021, 2022). We tested this expectation explicitly with our simulations $\mathcal{C}2$, $\mathcal{B}$, and $\mathcal{C}7$, which share the same CR current but saturate at different values of δB correlating with ξ_0.

The amplification described by Equation (9) can be explained with the following simple argument, based on the bottom panel of Figure 4. At saturation, the system achieves equipartition between: the three components of the thermal plasma pressure, the three components of the CR pressure, and the two transverse components of the amplified magnetic field. Since the initial free momentum is ξ_0, and since two of the eight final channels are in $P_{\rm B\perp}$, Equation (9) naturally ensues.

In principle, another channel in which the injected energy may go is the bulk motion; however, before saturation ($t \lesssim 10\gamma_{\rm max}^{-1}$), the thermal gas is not sped up much, while after saturation all of the energy goes into accelerating the coupled system of CRs+thermal plasma+magnetic fields (the top panel of Figure 4). Thus, the bulk motion is not an effective degree of freedom of the system, but rather the ultimate sink of all the energy injected after saturation.

Finally, we note that the effective CR drift becomes comparable with the Alfvén speed, eventually, but this happens *after* the magnetic field amplification has stopped because the system has run out of free momentum; the achievement of marginal stability can therefore be interpreted as a manifestation of the efficient coupling between CRs and magnetic fields (e.g., Zweibel 2017).

5. Discussion

Arguably, the main application of the nonresonant instability is for DSA in SNR shocks, as highlighted already by Bell (2004), who derived Equation (4) in the limit of the nonrelativistic drift of ultrarelativistic CRs with a power-law distribution in momentum $\propto p^{-4}$. In the same limit, Equation (8) would return a perpendicular amplified magnetic field

$$\left(\frac{\delta B_\perp}{B_0}\right)^2 = \frac{1}{4}\xi_0 \approx \frac{2}{3}\gamma_{\rm iso}\frac{n_{\rm cr}}{n_{\rm g}}\frac{v_{\rm d}^2}{v_{\rm A,0}^2}, \tag{10}$$

where we used $v_{\rm bst} \approx v_{\rm d}$ for nonrelativistic boosts.

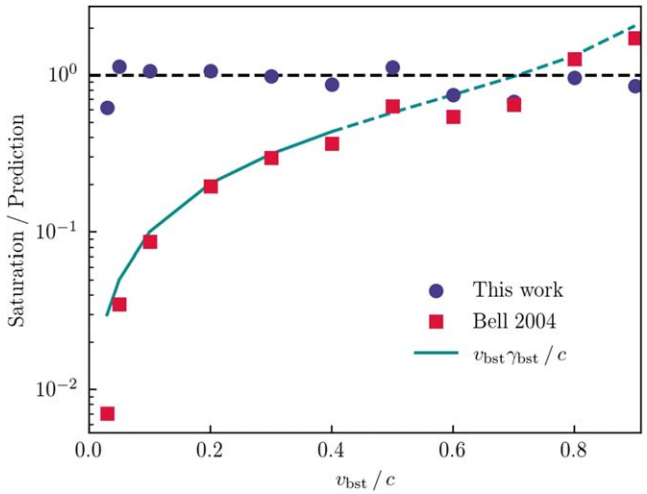

Figure 7. Saturated value of $(\delta B_\perp/B_0)^2$ measured in simulations over the one predicted by either Equation (4) (Bell 2004) or Equation (9); they differ by a factor of $v_{\rm bst}\gamma_{\rm bst}/c$, which means that Bell's prescription overestimates the measured values when the boost is nonrelativistic. We show the cases $\mathcal{H}6$–16, as these sample the $v_{\rm bst}$ parameter space.

This field is much smaller than the one provided by Equation (4), since $v_{\rm d} \sim v_{\rm shock} \ll c$ for SNRs. Figure 7 shows the ratio of $(\delta B_\perp/B_0)^2$ at saturation in simulations compared with either Bell's prescription (Equation (4)) or the new one (Equation (8)). Note that in Figure 7, we multiplied Bell's prescription by a factor $2/3$ in order to get an estimate of $\delta B_\perp^2$ rather than the total δB^2, assuming isotropic turbulence.

The current estimates of the maximum energy achievable in SNRs, which rely on Bell's saturation (e.g., Reville & Bell 2012; Bell et al. 2013), suggest that typical SNRs can accelerate particles up to maximum rigidities of fractions of a petavolt, a factor of a few to ten smaller than the rigidity of the CR knee. More precisely, the problem is not producing petaelectronvolt particles, but producing *enough* of them such that the overall CR spectrum rolls over at the knee (e.g., Cardillo et al. 2015; Cristofari et al. 2021, 2022; Diesing & Caprioli 2021).

While our saturation prescription (Equation (9)) seems to exacerbate this issue, thus challenging the idea that SNRs can be the sources of Galactic CRs, one has to remember that ahead of the shock there is a flux of escaping particles (e.g., Zirakashvili & Ptuskin 2008; Caprioli et al. 2009, 2010; Bell et al. 2013; Caprioli & Spitkovsky 2014b), which have momentum close to $p_{\rm max}$, i.e., the instantaneous maximum momentum. Such particles have a very anisotropic distribution that can be effectively described as a cold beam with $p_{\rm bst} \approx p_{\rm max}$ and $v_{\rm bst} \approx c$, but with number density $n_{\rm esc} \simeq \frac{v_{\rm sh}}{c} n_{\rm cr}$, with $n_{\rm cr}$ measured at the shock (at least for a p^{-4} CR spectrum; see, e.g., Caprioli et al. 2009; Bell et al. 2013). Hence, assuming isotropic turbulence, the total field, i.e., $\delta B^2 = \frac{3}{2}\delta B_\perp^2$, produced by escaping particles reads

$$\left(\frac{\delta B}{B_0}\right)^2 \approx \frac{3}{4}\frac{n_{\rm esc}}{n_{\rm g}}\frac{c\, p_{\rm max}}{m v_{\rm A,0}^2} \approx \frac{3}{4}\frac{n_{\rm cr}}{n_{\rm g}}\frac{v_{\rm sh} p_{\rm max}}{m v_{\rm A,0}^2}, \tag{11}$$

which is exactly Bell's prescription (Equation (4), modulo a factor of order unity). Eventually, our results do not quantitatively change the estimates of the maximum energy achievable in SNRs (e.g., Reville & Bell 2012; Bell et al. 2013;

Cardillo et al. 2015; Cristofari et al. 2021, 2022; Diesing & Caprioli 2021), although they suggest that most of the magnetic field amplification upstream of SNR shocks must be driven by the current in escaping particles, rather than by the current due to the anisotropy of CRs diffusing in the precursor. This also means that if the CR spectrum is steeper than p^{-4}, the saturated magnetic field may be smaller than the standard prediction and thus lead to smaller maximum energies, as pointed out, e.g., by Cristofari et al. (2022).

6. Conclusions

We have used controlled hybrid simulations to investigate the saturation of the Bell instability (Bell 2004, 2005) for a wide range of CR distributions, spanning from cold beams to hot-drifting cases (Figure 1 and Table 1). We used a suite of 1D, 2D, and 3D runs to assess the final amplitude of the self-generated magnetic field, and our main findings can be summarized as follows:

1. During the linear stage of the instability, the CR current is undisturbed by the small-wavelength waves that are excited at $k_{\rm max}$; when $\delta B/B_0 \gtrsim 1$, CRs start scattering and the amplitude of the magnetic field grows linearly rather than exponentially.
2. After about 10 growth times, the pressures in CRs, magnetic fields, and thermal plasma become comparable (Figure 4) and the instability saturates.
3. At saturation, CRs and thermal plasma are well coupled: the effective drift speed becomes comparable to the Alfvén speed in the amplified field and marginal stability is achieved (Figure 3).
4. In the asymptotic state, most of the magnetic power is not at the fastest-growing mode, but rather at larger scales, comparable to the CR gyroradius in the amplified field (see Figures 2 and 5).
5. While the growth rate depends on the CR current, the total magnetic field amplification that can be achieved depends on the momentum flux in CRs, generally parameterized by Equation (8). In particular, simulations suggest that the final pressure in transverse magnetic fields is ∼one-quarter of the initial CR pressure flux (Equation (9) and Figure 6).
6. The simulation-validated prescription (Equation (9)) for the saturated magnetic fields yields amplification factors *smaller* than the original prescription by Bell (Equation (4)), especially for nonrelativistic boosts (Figure 7).
7. The results above do not change the estimate of the maximum energy achievable in SNRs, where most of the field amplification is driven by the anisotropic beam of ultrarelativistic particles escaping upstream, rather than by CR diffusing in the shock precursor.

These results provide the first prescription, validated by self-consistent kinetic simulations, that can be used to estimate the total magnetic field amplification ensuing from an arbitrary distribution of anisotropic CRs, as long as electron physics is not important (i.e., that the current is not too strong to drive instabilities other than Bell's; see Niemiec et al. 2008; Bret 2009; Riquelme & Spitkovsky 2009) and the thermal plasma is relatively cold (e.g., Reville et al. 2008; Zweibel & Everett 2010). We defer the study of saturation in such systems to future works.

Quantifying the level of magnetic field amplification in SNRs is important not only for estimating the maximum energy achievable via DSA, but also the dynamics of the shock, the overall shock compression, and the slope of the accelerated particles (Caprioli et al. 2020; Haggerty & Caprioli 2020; Diesing & Caprioli 2021; Cristofari et al. 2022).

Acknowledgments

We thank the reviewer for the constructive comments. Simulations were performed on computational resources provided by the University of Chicago Research Computing Center and on TACC's Stampede2 through ACCESS (formally XSEDE) allocation (TG-AST180008). We wholeheartedly thank Ellen Zweibel, Pasquale Blasi, Elena Amato, and Lorenzo Sironi for interesting and stimulating discussions. This work of D.C. was partially supported by NASA through grants 80NSSC20K1273, 80NSSC18K1218, 80NSSC23K1481 and 80NSSC24K0173, and the NSF through grants AST-1909778, PHY-2010240 and AST-2009326, while the work of C.C.H. was supported by NSF FDSS grant AGS-1936393, and NASA grants 80NSSC20K1273 and 80NSSC23K0099.

Appendix
Effects of Simulation Dimensionality

In 2D hybrid simulations, we report an anisotropy in the transverse (self-generated) magnetic field. Specifically, for our 2D boxes in the x–y plane, we find that typically $B_z \gtrsim B_y$ and that the ratio of such transverse components may reach a factor of a few, depending on the simulation parameters. This makes it hard to choose which component of the magnetic field must be used to calculate the saturated value of the field. In quasi-1D boxes, i.e., when $L_y \ll L_x$ and $L_z = 0$, we find that at saturation, $B_y \sim B_z > B_x$ and that $B_x \sim B_0$, as expected. In 3D simulations, instead, we find that $B_y \sim B_z$, similar to the 1D case, and that the two components are comparable to the B_z one in the 2D box. These scalings are shown in Figure 8, where we compare simulations $\mathcal{D}1$, $\mathcal{D}3$, and $\mathcal{B}$. The former two are similar to our benchmark simulation $\mathcal{B}$, but with 1D and 3D boxes, respectively.

This test indicates that the B_z component in 2D simulations might be a good proxy for the behavior of both perpendicular components in more realistic 3D setups. However, the difference between $\delta B_\perp = (B_y^2 + B_z^2)^{1/2}$ and the proxy $\sqrt{2}B_z$ is only about 20%–30%. Therefore, we use $\delta B_\perp$ to quantify the

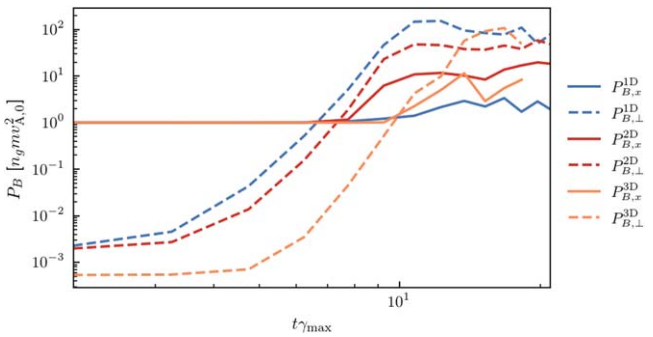

Figure 8. Time evolution of the parallel (solid) and perpendicular (dashed and dotted) components of the magnetic field for the benchmark run, in 1D, 2D, and 3D configurations (runs $\mathcal{D}1$, $\mathcal{B}$, and $\mathcal{D}3$); note that run $\mathcal{D}_1$ has $50d_i$ in the y-direction, so is not exactly 1D, which allows for a B_x that is not strictly constant. The B_z component in 2D is a good proxy for both transverse components in full 3D setups.

field at saturation in this paper, keeping in mind that this might be slightly underestimating the actual value in full 3D. Such an uncertainty is also conveyed by the yellow envelope around the theoretical prescription (Equation (8)) in Figure 6.

ORCID iDs

Georgios Zacharegkas https://orcid.org/0000-0002-2890-6758
Damiano Caprioli https://orcid.org/0000-0003-0939-8775
Colby Haggerty https://orcid.org/0000-0002-2160-7288
Siddhartha Gupta https://orcid.org/0000-0002-1030-8012
Benedikt Schroer https://orcid.org/0000-0002-4273-9896

References

Achterberg, A. 1983, A&A, 119, 274
Amato, E., & Blasi, P. 2009, MNRAS, 392, 1591
Bell, A. R. 1978, MNRAS, 182, 147
Bell, A. R. 2004, MNRAS, 353, 550
Bell, A. R. 2005, MNRAS, 358, 181
Bell, A. R., & Lucek, S. G. 2001, MNRAS, 321, 433
Bell, A. R., Schure, K. M., Reville, B., & Giacinti, G. 2013, MNRAS, 431, 415
Blandford, R. D., & Ostriker, J. P. 1978, ApJL, 221, L29
Blasi, P., Amato, E., & Caprioli, D. 2007, MNRAS, 375, 1471
Blasi, P., Amato, E., & D'Angelo, M. 2015, PhRvL, 115, 121101
Bret, A. 2009, ApJ, 699, 990
Bykov, A. M., Osipov, S. M., & Ellison, D. C. 2011, MNRAS, 410, 39
Caprioli, D., Blasi, P., Amato, E., & Vietri, M. 2009, MNRAS, 395, 895
Caprioli, D., Haggerty, C. C., & Blasi, P. 2020, ApJ, 905, 2
Caprioli, D., Kang, H., Vladimirov, A. E., & Jones, T. W. 2010, MNRAS, 407, 1773
Caprioli, D., & Spitkovsky, A. 2013, ApJL, 765, L20
Caprioli, D., & Spitkovsky, A. 2014a, ApJ, 783, 91
Caprioli, D., & Spitkovsky, A. 2014b, ApJ, 794, 46
Caprioli, D., & Spitkovsky, A. 2014c, ApJ, 794, 47
Caprioli, D., Zhang, H., & Spitkovsky, A. 2018, JPlPh, 84, 715840301
Cardillo, M., Amato, E., & Blasi, P. 2015, APh, 69, 1
Cristofari, P., Blasi, P., & Caprioli, D. 2021, A&A, 650, A62
Cristofari, P., Blasi, P., & Caprioli, D. 2022, ApJ, 930, 28
Crumley, P., Caprioli, D., Markoff, S., & Spitkovsky, A. 2019, MNRAS, 485, 5105
Diesing, R., & Caprioli, D. 2021, ApJ, 922, 1
Gargaté, L., Bingham, R., Fonseca, R. A., & Silva, L. O. 2007, CoPhC, 176, 419
Gargaté, L., Fonseca, R. A., Niemiec, J., et al. 2010, ApJL, 711, L127
Gupta, S., Caprioli, D., & Haggerty, C. C. 2021, ApJ, 923, 208
Haggerty, C., Caprioli, D., & Zweibel, E. 2019, ICRC (Madison, WI), 36, 279
Haggerty, C. C., & Caprioli, D. 2019, ApJ, 887, 165
Haggerty, C. C., & Caprioli, D. 2020, ApJ, 905, 1
Kobzar, O., Niemiec, J., Pohl, M., & Bohdan, A. 2017, MNRAS, 469, 4985
Kulsrud, R., & Pearce, W. P. 1969, ApJ, 156, 445
Lagage, P. O., & Cesarsky, C. J. 1983, A&A, 118, 223
Landau, L., & Lifshitz, E. M. 1987, Fluid Mechanics (2nd ed.; Amsterdam: Elsevier)
Lucek, S. G., & Bell, A. R. 2000, MNRAS, 314, 65
Malovichko, P., Voitenko, Y., & De Keyser, J. 2015, MNRAS, 452, 4236
Marcowith, A., van Marle, A. J., & Plotnikov, I. 2021, PhPl, 28, 080601
Marret, A., Ciardi, A., Smets, R., & Fuchs, J. 2021, MNRAS, 500, 2302
Marret, A., Ciardi, A., Smets, R., Fuchs, J., & Nicolas, L. 2022, PhRvL, 128, 115101
Matthews, J. H., Bell, A. R., Blundell, K. M., & Araudo, A. T. 2017, MNRAS, 469, 1849
Niemiec, J., Pohl, M., Stroman, T., & Nishikawa, K.-I. 2008, ApJ, 684, 1174
Ohira, Y., Terasawa, T., & Takahara, F. 2009, ApJL, 703, L59
Reville, B., & Bell, A. R. 2012, MNRAS, 419, 2433
Reville, B., & Bell, A. R. 2013, MNRAS, 430, 2873
Reville, B., Kirk, J. G., Duffy, P., & O'Sullivan, S. 2007, A&A, 475, 435
Reville, B., Kirk, J. G., Duffy, P., & O'Sullivan, S. 2008, IJMPD, 17, 1795
Riquelme, M. A., & Spitkovsky, A. 2009, ApJ, 694, 626
Schroer, B., Pezzi, O., Caprioli, D., Haggerty, C., & Blasi, P. 2021, ApJL, 914, L13
Schroer, B., Pezzi, O., Caprioli, D., Haggerty, C. C., & Blasi, P. 2022, MNRAS, 512, 233
Stroman, T., Pohl, M., & Niemiec, J. 2009, ApJ, 706, 38
Weidl, M. S., Winske, D., & Niemann, C. 2019a, ApJ, 872, 48
Weidl, M. S., Winske, D., & Niemann, C. 2019b, ApJ, 873, 57
Winske, D., & Leroy, M. M. 1984, JGR, 89, 2673
Zacharegkas, G., Caprioli, D., & Haggerty, C. 2019, ICRC (Madison, WI), 36, 483
Zacharegkas, G., Caprioli, D., Haggerty, C., & Gupta, S. 2022, ICRC (Berlin), 37, 483
Zirakashvili, V. N., & Ptuskin, V. S. 2008, ApJ, 678, 939
Zirakashvili, V. N., Ptuskin, V. S., & Völk, H. J. 2008, ApJ, 678, 255
Zweibel, E. G. 1979, in AIP Conf. Ser. 56, Particle Acceleration Mechanisms in Astrophysics, ed. J. Arons, C. McKee, & C. Max (Melville, NY: AIP), 319
Zweibel, E. G. 2017, PhPl, 24, 055402
Zweibel, E. G., & Everett, J. E. 2010, ApJ, 709, 1412